On the Hunt for Dark Photons: Improving the Tracking of Vertical Drift Chambers

BY

Dylan J. Linthorne

A thesis submitted to the

Department of Physics and Astronomy

Saint Mary's University

in partial fulfillment of the requirements for the

Bachelor of Science degree

with Honours

May, 2016

(Department of Physics and Astronomy, Dr. A.J. Sarty supervising faculty)

.....

.....

.....

.....

ABSTRACT

The current standard model (SM) of particle physics does not account for the dark matter (DM) presence within the universe. A theoretically proposed new force, governed by a $U(1)$ Boson, has been an ongoing subject of experimental searches as a bridge between SM particles and DM models. An experimental search for the Dark Photon/A' Boson will commence in experimental Hall A at Jefferson Lab some time in 2016-17. The Hall A High Resolution Spectrometer (HRS) will be used in attempt to detect the A' Boson with masses $O(50MeV - 500MeV)$ as it decays into e^-e^+ pairs. The high luminosity required for the experiment creates HRS trigger rates of 5 Mhz, which presents a problem for the tracking efficiency of the resultant e^-e^+ pairs. The HRS uses four vertical drift chambers (VDC) to detect particle tracks by means of gas ionization. Previously, VDC signal data has been analyzed using an older "brute force" algorithm which was appropriate at much lower particle rates (lower Background). This presentation reports on a new VDC algorithm created to better handle higher particle traversal rates, and tested using previously obtained high-rate test data. This new analysis identifies a set of 'miss match' parameters δS, which enable local cuts on background tracks. The new method identifies a final good track by constructing global tracks from multiple VDCs and minimizing their χ^2. Global tracking efficiencies are increased by the addition of these new local track constraints/cuts, which will meet the needs of the Dark Photon/ A' Boson experimental search.

ACKNOWLEDGMENTS

Firstly, I would like to thank Dr. Adam Sarty for giving me the opportunity of assisting him in particle physics research. Secondly, Nathan J. Murtha for his assistance in my research. Thirdly, Bogdan Wojtsekhowski for his methods and insights which laid the groundwork for my thesis project. Finally, I would like to thank Sara Hollett for keeping me sane over the perils of my research difficulties.

Contents

List of Figures

List of Tables

GLOSSARY

ADC	Analog-to-Digital Converter
APEX	A' Boson Experiment
CEBAF	Continuous Electron Beam Accelerator Facility
DM	Dark Matter
EM	Electromagnetic
HRS	High Resolution Spectrometer
JLab	Jefferson National Laboratory
MWPC	MultiWire Proportional Counter
PID	Particle Identification Detector
PMT	PhotoMultiplier Tube or also Phototube
QCD	Quantum ChromoDynamics
QED	Quantum ElectroDynamics
QFT	Quantum Field Theory
RMSE	Root Mean Square Error
ROC	ReadOut Control
SN	Signal-to-Noise
SM	Standard Model
TDC	Time-to-Digital Converter
TS	Trigger Supervisor
TTD	Time-to-Distance
UV	Upper-Lower
VDC	Vertical Drift Chambers
WIMP	Weakly Interacting Massive Particles

Chapter 1

Jefferson Lab/ Hall A

The Thomas Jefferson National Accelerator Facility (JLab) is concerned with studying the properties of atomic interactions through scattering processes. JLab is designed to probe nuclei through fixed target scattering experiments. It is one of the first laboratories to create their electron beam through superconducting radio frequency (SFR) technology. Through SFR enhancements throughout the years Jlab can currently obtain beam energies up to 12GeV [Mur15]. This allows for the study of sub-atomic physics within and around the perturbative (low energy) and non-pertubative (high energy) quantum chromodynamics (QCD) interface.

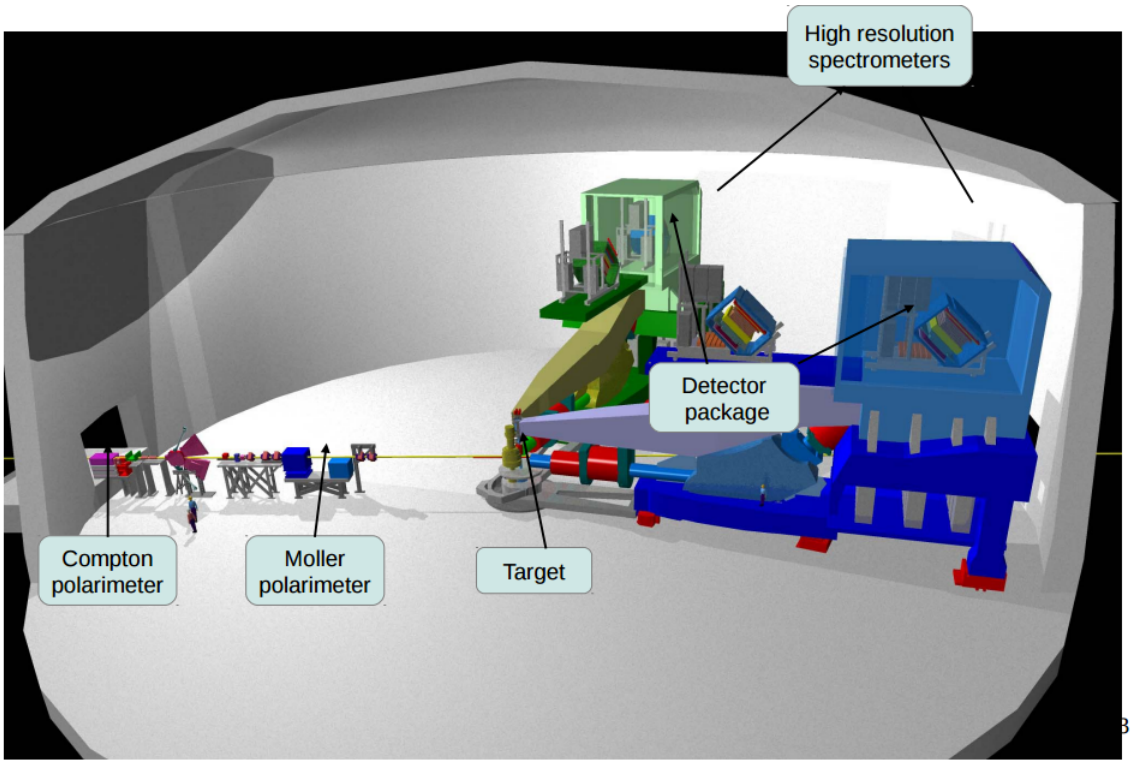

Figure 1.1: Hall A experimental hall, displaying the configuration of the HRS.

The electron beam is produced by the Continuous Electron Beam Accelerator Facility (CEBAF) and is fed to one of four experimental halls. The beam lies incident on a chosen target or radiator and produces resultant particles through electromagnetic interactions with either a sub-nuclear component (e.g. proton or neutron) or a sub-nucleonic component(e.g. virtual pion, or quark), depending on the energy. Hall A is one of four experimental halls within Jlab. The hall comprises of two high resolution spectrometers (HRS). The spectrometers have a small angular acceptance, but can rotate over a wide angular range about the target's center. The resultant particles are collimated through a set of magnets attached to the HRS. The HRS hosts dipole (D) and quadrapole magnets (Q) configured in the following order (QDQQ) [J. 03]. The dipole magnet is used to bend the trajectory of the particles towards the detector packages. A charged particle traversing within a magnetic field will be bent along an arc dependant on the strength of the field, and the momentum of the particle. For the extremely high momenta of these particles a large dipole magnet is used to produce the needed magnetic field. The quadrapole magnets are used to focus and collimate the particle streams. The magnet placement is optimized to provide the best combination of high resolution in momentum determination and angle of particle track.

The HRS is fitted with a detector package composed of two vertical drift chambers (VDC), two Scintillator panels, and a Cherenkov detector. The VDCs are used to reconstruct the track geometry which is crucial in determining scattering angles and particle momenta. The sintillator panels are only used for triggering events since they are designed to be completely penetrated by the particles. The Chrenkov detector is used as a particle identification detector (PID), which distinguishes the particles by their charge to mass ratios.[J. 03]

1.1 Vertical Drift Chambers (VDC)

The Hall A vertical drift chambers work as multiwire proportional counters. Relativistic charged particles are collimated from the magnets and sent to the VDCs with a nominal angle of 45°. The chamber is set at a potential difference of $4.0kV$ between a set of anode wires and the cathode plates. The chamber is filled with gas which is ionized by the flux of charged particles. The ion's drift times are used to reconstruct the particle track geometry. [K.G00]

Each HRS (right and left) carry a pair of VDCs, one lower VDC and one upper VDC. The top chamber plates for each pair are referred to as the V-planes and U-planes for the bottom plates. The separation between each VDC's U and V planes is 26mm. The separation between the V-planes of the lower and upper VDC is 335mm such as in Figure 1.2.

The VDCs contain a mixture of gasses (argon and ethane). Each (UV)-plane consists of an array of sense wires. The sense wires are placed 45° with respect to the other plane as in Figure 1.2. The distance between adjacent sense wires is $4.24mm$ with a total of 368 wires per plane. The separation between wires does not limit the the positional and angular resolution. The reason for the two 45° adjacent planes is to increase the resolution by the finer grids when combined.[J. 03]

1.1.1 Gasses

The chambers are continuously pumped with a composition of two gasses, argon (62 %) and ethane (38 %). The main purpose of the gas within the VDC is to be ionized by the particle tracks. Noble gasses are highly sensitive to becoming ionized due to their complete valence shell configuration.[Lea96]

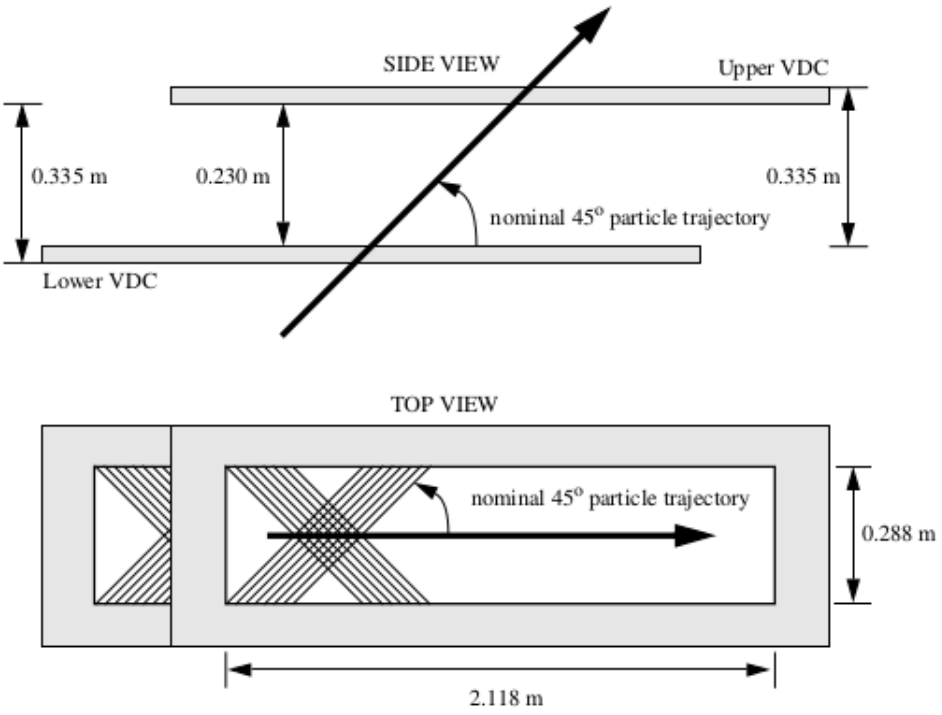

Figure 1.2: Two Vertical Drift Chambers and their corresponding dimensions. The chamber's wire planes are arrayed 45° with respect to the other. The cross-hatching of two wire chambers increases the position resolution of the tracks.[J. 03]

False avalanches occur when argon becomes excited and discharges radiatively. Introducing polyatomic molecules within drift chambers has lowered the rate of false signals. Polyatomics have many degrees of freedom in their motion which correspond to specific rotational and vibrational energy bands. Ethane's rational and vibrational bands match the energies of discharging argon. Ethane will dissipate transmitted energy by collisional interactions.[Sau76]

1.1.2 Electric Feild lines

The VDCs do not produce "perfect parallel" plate electric fields. The fields slightly change near the sense wires. These electric fields will produce lines perpendicular to the (UV)-planes forcing the ions to be collected at each end. A parallel plate at a

constant voltage will produce constant parallel electric field lines, perpendicular to the chamber plates. The electric field effects of the cylindrical anode wires must be accounted for when considering ion mobility. Maxwell's equations can be solved for a cylindrical capacitor and the corresponding electric field is given by the following Eequation (1.1) [Gri04].

$$\hat{E}(r) = \frac{CV}{2\pi\epsilon}\frac{1}{r}\hat{r} \tag{1.1}$$

where r is the distance from the anode wire, V is the voltage beween the anode wire and the cathode plate, and C is the capacitance of the configuraiton.The Electric field around the anode wire gives a $\frac{1}{r}$ radial dependence for arbitrary capacitance. The electric non constant electric field will affect the forces felt on the ions and correspondingly affect their motion. The potential map can be derived by integrating the field around a surface of constant radius

$$\phi(r) = -\frac{CV}{2\pi\epsilon} ln(\frac{r}{a}) \tag{1.2}$$

Where a is the radius of the wire. The potential map is still radially dependant. In Figure 1.3 the equipotential lines throughout the VDC can be seen. The lines are relatively constant further away from the anode wires where the field diverges.

1.2 Data Acquisition

The data acquisition protocol is CODA for CEBAF on-line data acquisition system. The raw signals from various detectors are amplified and sent to an analog to digital converter (ADC). The ADC measures the integrated charge from the raw signals. If the signal amplitude is higher then a discriminator threshold, a logical signal is sent to the array of Time to Digital Converters (TDC) and scalar information is saved. The

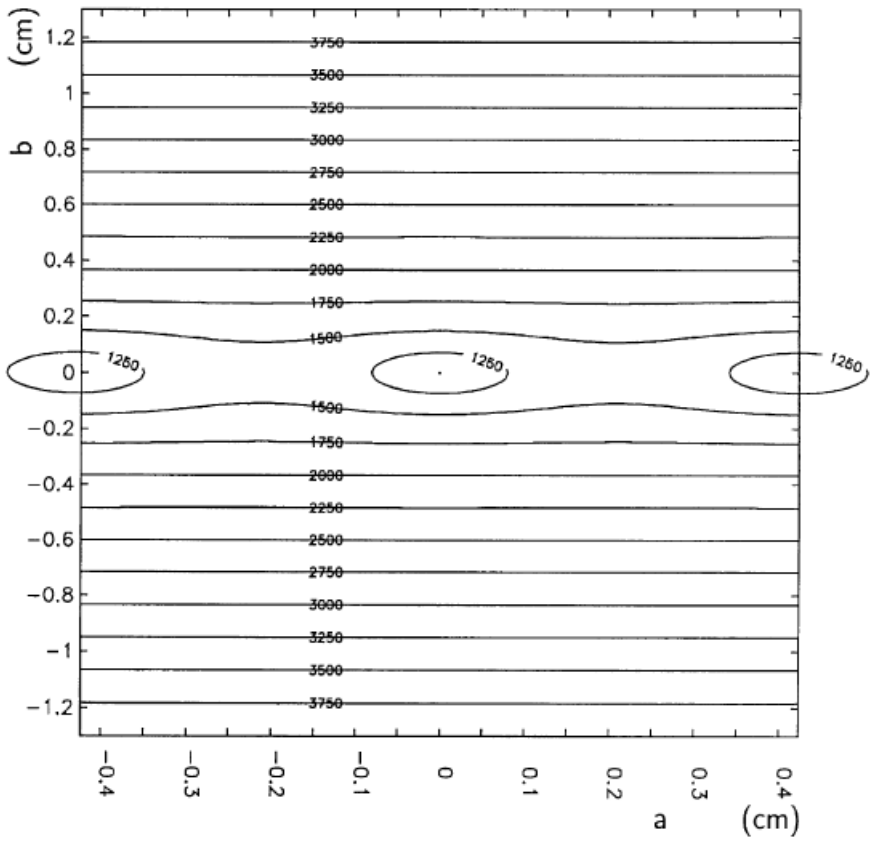

Figure 1.3: Position dependent equipotential map for the VDC. The sense wires change the field from constant (parallel plate) to a radial dependant field (cylindrical). [Lea96]

TDCs are contained in various crates and a control module ROC (readout control) is used to identify the crate's TDC by channel [J. 03].

The trigger supervisor (TS) decides which events are recorded and which are rejected based on the triggering system in use. There are eight input trigger scalers $(T1, T2, T3, T4, T5, T6, T7, T8)$ [J. 03]. If the trigger signal is accepted it is sent to ROC and the data is read from the module. Only one signal can be read at a time. While a signal is being read, no other signals are allowed to be read which causes dead-times throughout the data acquisition process.

The VDC will be working at high rates for the APEX experiment, with the VDCs

experiencing a constant ionization current of about $5\mu A$. The VDCs use a LeCroy Amplifier-discriminator cards 2735DC. The trigger signal rates will be around $5Mhz$. A projected 1.75 accidental tracks will occur per event at the high rates [J.D10]. Further reduction of accidentals will have to be implemented.

1.3 Hall-A Analyzer/CERN Root

A commonly used analysis tool in particle physics is the Root CERN toolkit. It is an interpreted toolkit based on the C++ programming language. Root is a program of abstract hierarchical particle physics objects. For example Root allows the user to define a four-vector object which contains operations and transformations in terms of (E, p_x, p_y, p_z) or (t, x, y, z) vectors. The universal use of Root throughout many particle physics labs has increased its omnibus of tools ranging from polarization classes to asymmetry calculations.

The collaboration at Hall-A has created an extension to Root characteristic for the Hall-A detectors. The Hall-A Analyzer has built in objects for each detector which inherits from other root detector classes. The addition of these unique Hall-A detector classes allows for easy analysis of the signal data received by each detector. This thesis uses the analyzer's vertical drift chamber classes as well as other classes for signal analysis.

Chapter 2

EXPERIMENT

2.1 The Standard Model

The Standard Model (SM) of particle physics is a testament of our understanding of the microscopic interactions of particles. Gravity is ignored within the standard model due to its large scale force having little effect in the microscopic regime of particle physics. The SM is a phenomenological theory of particle physics within the framework of a quantum field theory (QFT). The theory incorporates the fundamental forces of physics (strong, weak and EM) within a single model. Even though it has the ability of describing physical interactions with astonishing precision, most physicists believe the SM is a low energy limit of a more fundamental theory.

Fundamental particles are characterized by quantities such as mass, spin, charge and other quantum numbers. The particles described within the SM are subdivided into two classes. Fermions, which have half-integer spins, and bosons, which have multiple integer spin. In the case of fermions, particles can be subdivided into leptons and quarks. Electrons e^- and electron neutrinos ν_e are cases of leptons while for quarks we have up (u) and down (d) quarks, for example [Lan14]. There exists a hierarchy of particles within the standard model. Three groups of particles mimic each other in all quantum numbers (S,q,Y..) except in mass. Each one of the hierarchy groups is distinguished by two leptons and two quarks. An example is the second generation group consisting of a muon μ^-, muon neutrino ν_μ and two quarks, top (t) and bottom (b). The family of fermions is shown in Figure 2.1 with charge and mass

information.

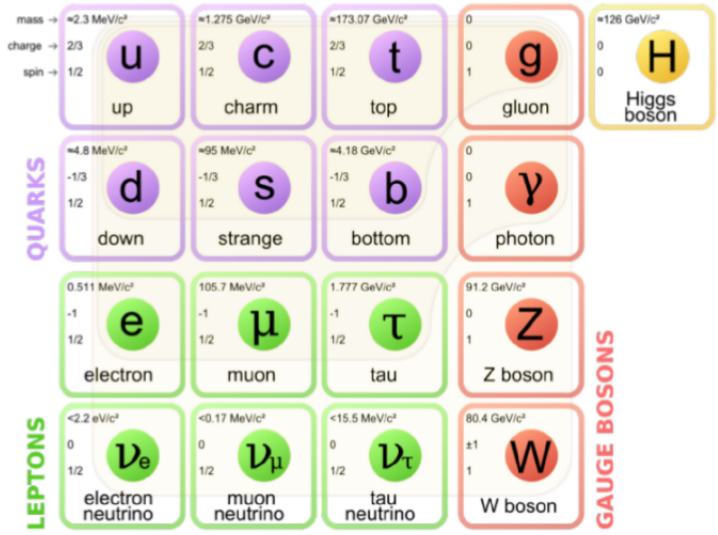

Figure 2.1: The particles of the Standard Model of particle physics. The associated quantum numbers and mass are given for each hierarchy as well as bosons. [Lan14]

The interactions between particles within the SM are governed by the exchange of four force carriers known as gauge bosons. The photon γ interacts via EM charges, W and Z bosons interact via weak charges and the gluons g interact via the strong charge. The photon and gluons have a mass of zero due to preserving special types of symmetries. The W and Z bosons have a non-zero mass which has been explained by continuous symmetry breaking by interactions with the Higgs field [Rom14]. The symmetry breaking occurs at high energies where the weak and EM forces are indistinguishable and unified into a single general electroweak force. The continuous symmetry breaking of the electroweak force gives mass to the SM particles proportional to the strength of the electroweak scale.

The SM is a quantum field theory therefore it must be equally represented in terms of fields and not just particles. A field $\phi(x)$ is defined by the space-time coordinates, in this case the Minkowski metric defines our space time $(x^0, -x^1, -x^2, -x^3)$. The field is an object which permeates the space-time it is embedded in. Particles are emergent

from interactions with their respected fields. Quantum feild theories are formulated under an action principle S with a defined Lagrangian density. The formulation is historically considered the Freymen path integral for a given actions S [Buc06].

$$S = \int d^4x \mathcal{L}(x) \tag{2.1}$$

The integration is done in four-space weighted by the Lagrangian density of the SM. The Lagrangian density of the standard model is a complicated sum of fields and their propagator's charges q_i. The power of the action formulation is that the Lagrangian density $\mathcal{L}$ of the system (in this case all of particle physics) is just the sum of the Lagrangians of its parts. In the case of constructing a Lagrangian for a given interaction Feynman diagrams are used to find the amplitudes/coupling coefficients of the fields.

In field theories of classical mechanics and quantum mechanics, it is known that the action principle reveals conservation laws. The invariance of the Hamiltonian $\hat{\mathcal{H}}$ defined by a system's action S will produce conservation laws of the system. The conservation of energy is due to time invariance of the Hamiltonian of the system. It was Emmy Noether, a brilliant mathematician, who proved the equivalence of continuous symmetries and conservation laws. Neother's theorem expresses the relationships between a field theory's conservation laws and underlining geometric as well as abstract symmetries [Gol01]. From Neother's Theorem the SM can then be represented in terms of global as well as local (gauge) symmetries instead of just a action formulation. The group theory symmetries which govern the SM are subgroups of the Poincare groups $\mathcal{P}$ and Lie groups. Quantum mechanics tells us that the symmetries

must commute with the Hamiltonian.

$$[\hat{A}, \hat{\mathcal{H}}] = 0 \tag{2.2}$$

Since the symmetries are continuous by Neother's theorem and by the previous restrictions, the only possible allowed symmetries are Special Unitary $SU(N)$ and Unitary $U(1)$ symmetries [Gol01]. Within the SM gauge bosons are represented by generators of these symmetries. The photon is of $U(1)$ symmetry. The $W^{\pm}$ and Z are of $SU(2)$ and the gluons are of $SU(3)$. The respective conserved charges are electric (q), isospin (Y) and colour (c). Thus the standard model as we understand to this day is the tensor product (direct product) of these irreducible symmetry groups [Rom14].

$$G_{sm} = U(1) \otimes SU(2) \otimes SU(3) \tag{2.3}$$

2.1.1 Standard Model Extensions/ Dark Photon

The Standard model has shown its ability to describe the physics of particle interactions thus far, although many theorists are attempting to look at possible extensions beyond the scope of the standard model. Particles which are theorized but have not been detected by current particle detectors comprise what is called the 'hidden sector'. The gauge symmetries discussed in the previous section act as constraints on new theorized hidden sector particles and their possible interactions with the currently established SM.

A new vector boson has been debated by theorists as a candidate for new SM extensions. This A' boson would act as a new force carrier under a new conserved charge (dark charge) [Ree10]. The impetus for such a theory is based on the unexplained observations of dark matter particles. Previous models of dark matter particles included

Table 2.1: Guage Bosons and their forces.

Gauge Boson	Force	Charge
A' (Dark Photon)	Dark	?
γ (photon)	EM	q
W, Z	Weak	Y
g (Gluons)	Strong	c

weakly interacting massive particles (WIMPs), although after decades of searching no detection of WIMP-like particles has occurred. Current models now change their scopes of dark matter interactions through a new force with a force carrier/mediator being the dark photon. The A' photon has potential of being this sought after dark photon.

The A' boson is a vector boson, meaning its symmetry is under $U(1)$, such as the photon. Constraints from Chiral, and Lorentz symmetry leave only one possible interaction portal with a SM particle ϕ. This interaction portal has a specific Lagrangian density [Bjo09].

$$\delta\mathcal{L} = g' A'_\mu \bar{\phi}\gamma^\mu \phi \tag{2.4}$$

Where g' is the coupling strength with the standard model particles and A'_μ is the $A\prime$ vector field. The models allow the A' boson to interact with both electrons and muons through a proposed mixing interaction called kinetic mixing [Che09]. The specific Lagrangian for kinetic mixing of the A' with the electromagnetic particles is defined in equation (2.5).

$$\delta\mathcal{L} = \frac{\epsilon_Y}{2} F'_{\mu\nu} F_Y^{\mu\nu} \tag{2.5}$$

The interaction is in terms of the field strength tensors of both the A' boson and the electroweak field $F'_{\mu\nu}, F_Y^{\mu\nu}$. Analogous to the electromagnetic field strength tensor

being in terms of the vector potential, $F_{\mu\nu}$ can be decomposed in terms of the A' vector field $F_{\mu\nu} = \partial_\mu A_{nu} - \partial_\nu A_{mu}$

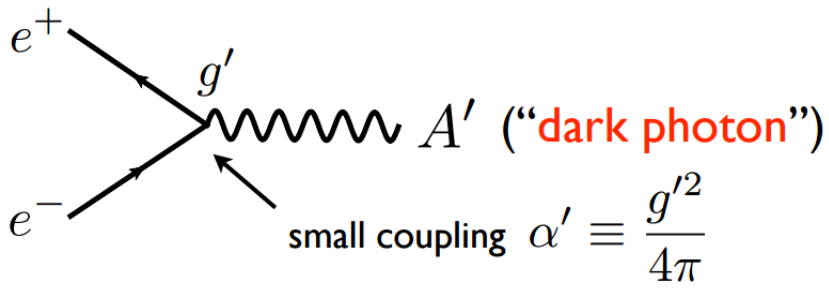

Figure 2.2: Vertex for the A' Boson/Dark Photon in terms of e^-e^+ pairs. [J.D10]

An example vertex interaction of the A' with electron-positron pair is shown in figure 2.2. The electron-positron pair will weakly couple with the A' with strength proportional to its coupling $\alpha = \frac{g'^2}{4\pi}$. The extension of this new vector boson will be added to the available global symmetries of the SM by another unitary $U(1)$ symmetry [Ber13]:

$$G_{ext} = U(1) \otimes SU(2) \otimes SU(3) \otimes U(1)_{A'} \tag{2.6}$$

2.2 A' Boson Experiment (APEX)

The detection of the A' boson has been an ongoing search at various particle accelerator facilities. The advantage of fixed target particle labs such as Jlab is the increased luminosity of particles. A large luminosity beam corresponds to more triggered events within a given time interval. Having such large event/triggering rates against a fixed target allows for precise measurements in low coupling regimes of particle physics [J.D10]. The low probability of a quantum mechanical event of interest will be overshadowed by the shear number of interaction opportunities per unit time with a high

luminosity beam, which increases the possible statistics of the measurements. The A' Boson Experiment (APEX) is planned to commence at some time during 2016/2017 within Hall-A. A test run was done using low trigger rates with very little statistics. The goal of the test run was to prove the capability of the detectors to work within the refined resolutions/constraints of the experiment.

2.2.1 Parameter Space

APEX will attempt to detect the A' by searching through the unseen parameter space of mass and couplings. The experiment will have a sensitivity for couplings at $\frac{\alpha'}{\alpha} \approx (6-8) \times 10^{-8}$ where the coupling is normalized by the fine structure constant (EM coupling). The mass sensitivity of APEX is within a range of $(50-500)$MeV. These constraints allow the observation within a large section of the parameter space, shown in Figure 2.3.

A specific decay channel will be the subject of observation for possible A' detection. A Tungsten target is used as a radiator alongside the Hall-A HRS. The reaction channel is a Bremsstrahlung-like interaction. Bremsstrahlung is German for "braking radiation", and is the interaction of a charged particle decelerating near an ion. The charged particle, e^- or e^+ will be decelerated by the Coulomb attraction felt by the ion [J.D10]. Since the electron, previously on a linear trajectory, is forced into a centripetal arc, the energy loss will be proportional to the strength of the coulomb attraction. If the ion is massive relative to the e^- it will not move therefore releasing a photon instead, conserving both energy and momentum. The Bremsstrahlung-like channel shown in Figure 2.4 is similar except an A' is radiated away instead of a photon.

The probability of producing an A' is manifested within the interaction cross-section σ. The cross section of classical Bremsstrahlung is inversely proportional to

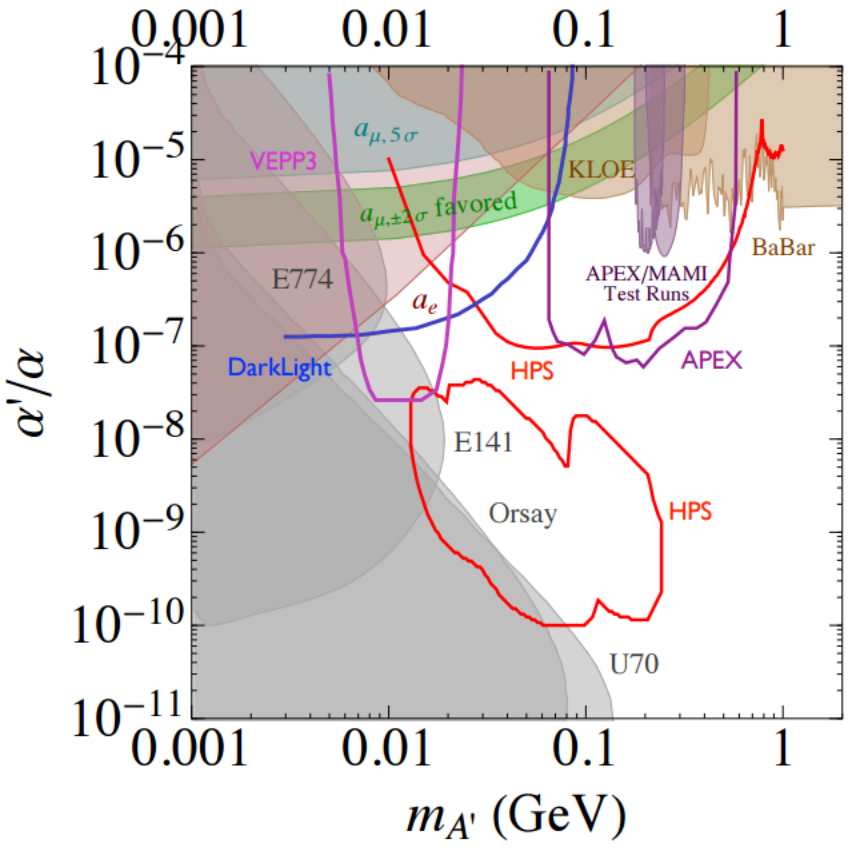

Figure 2.3: Mass-coupling parameter space for the A' boson. The proposed regime in which APEX is designed for is compared with previous and future experiments. [J.D10]

the mass of the incoming particle, which is why low mass e^-, e^+ are ideal. Tungsten was used as the target to increase the relative mass difference between the probe particle and the target [Jen13]. The Bremsstrahlung-like decay channel has a total cross section shown in equation (2.7).

$$\sigma \approx 100\ pb\ (\frac{\epsilon}{10^{-4}})^2(\frac{100MeV}{m_{A\prime}})^2 \tag{2.7}$$

2.2.2 Big Picture

The Hall-A HRS spectrometers will be placed in optimal configuration to receive the largest flux of scattered particles. The A' boson generated from interactions

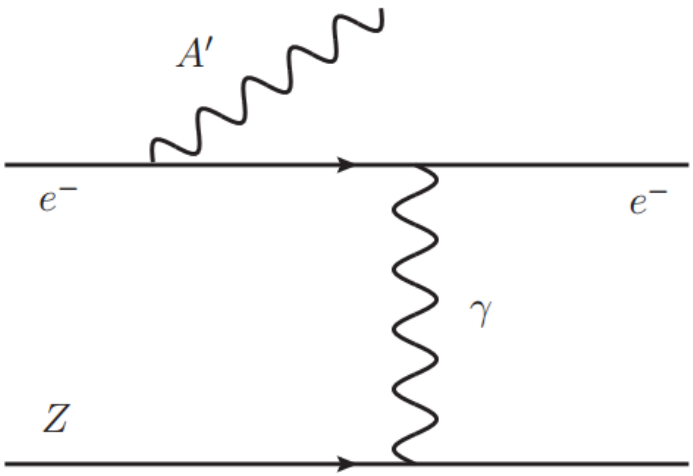

Figure 2.4: Bremsstrahlung-like interaction channel producing radiation of a A' boson. [Jen13]

is expected to decay into e^-e^+ pairs. Each HRS will collimate both the positron or electron and send them to their respective detector packages. The Cherenkov detectors will be used to identify which particle is produced within each event. A coincidence trigger will be set between the two HRS to locate possible e^-e^+ pairs produced from the same scattering.

A particle's energy/mass can be reconstructed by using information about the decayed daughter particles. This method of particle reconstruction is known as the missing mass or invariant mass. Invariant masses are independent of the frame of reference for the detected particles. The invariant mass reconstruction of the e^-e^+ will describe all of the possible energies/masses of the particle from which it decayed. Theoretical models of QED have established the possible SM contributions to the invariant mass of e^-e^+. APEX will be using equation (2.8) to find the invariant mass in the hopes to detect a new resonance within the distribution of energies beyond the expected standard SM invariant mass distribution.

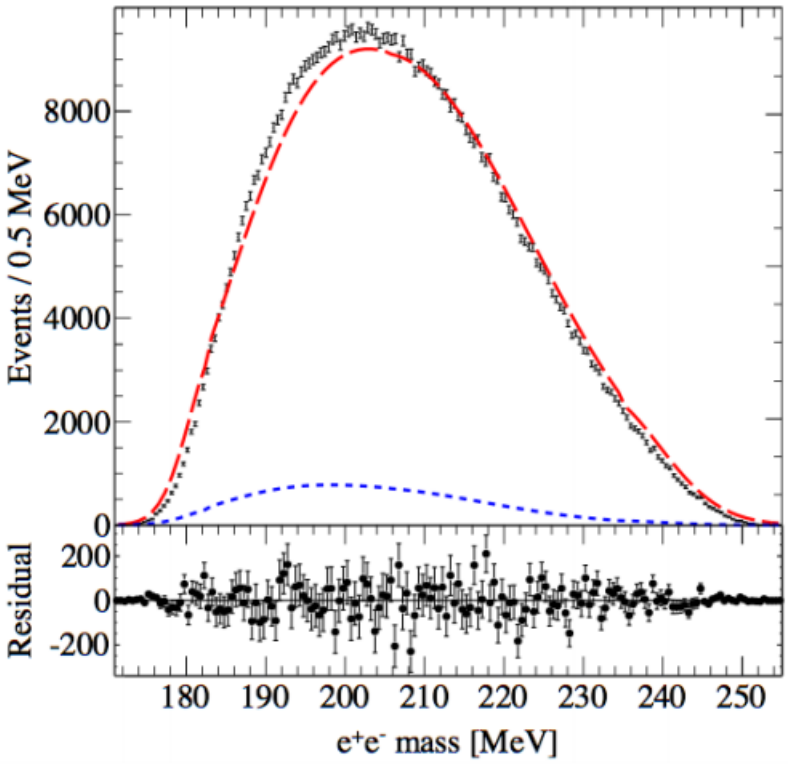

Figure 2.5: APEX test run data of the e^-e^+ invariant mass. The data is overlaid by the expected QED background and accidentals. The test run data is too low of a resolution to infer any resonances within the residuals. [J.D10]

$$m \approx 2m_e^2 + p_- p_+((\theta_- + \theta_+)^2 - \theta_- \theta_+ \phi^2) \tag{2.8}$$

Where (p, θ) are the momentum and scattering angle of the particles measured in the lab frame. The positive and negative subscripts denote each particle and ϕ is the angle between the two HRS. The invariant mass profile experimentally known from QED backgrounds is shown in red in Figure 2.5, while the accidental rates of false events is estimated by the blue line. The total expected invariant mass is plotted over the APEX test run data within Figure 2.5. The low statistics of the test run limit the resolution for any resonances to be detected. The resolution in the invariant mass equation is highly dependent on the scattering angle resolution. The optimization of

the VDCs for APEX will be the topic of the rest of this thesis. A new algorithm was designed to increase the efficiency of its track reconstruction without compromising the needed angular resolution.

Chapter 3

Vertical Drift Chambers

3.1 Theory of VDC/MWPC

Relativistic charged particles interacting with noble gasses is the key mechanism of detection for the VDCs. The particles primarily interact electromagnetically, thus strong and weak interactions are not considered. The various electromagnetic reaction channels include Bremsstrahlung, electronic transitions and Chrenkov radiation. [Sau76]

The traversing charged particle will exchange its energy with the gas by means of particle ionization. The traversing particle's energy loss is defined by the Bethe-Block formula [Wec96].

$$\frac{dE}{dX} = -\frac{2\pi N z^2 e^4}{mc^2}\frac{Z}{A}\frac{\rho}{\beta^2}(ln(\frac{2mc^2\beta^2 E_M}{I^2(1-\beta^2)} - 2\beta^2) \tag{3.1}$$

Equation (3.1) expresses the average differential energy loss per unit length, and is corrected for relativistic Coulomb interactions. The energy loss is due to ionization of the gasses atoms/molecules. This interaction will produce a pair of negative and positive ions. The negative ions will drift towards the wires and continue to interact with the gas. Second ionization is when the drifting negative ions begin to ionize the gas again. This ionization multiplicity process is referred to as avalanching [Wec96]. The constant electric field causes the drift ions to move with constant velocity. The radial electric field near the sense wires causes the mobility of the ions to increase

and produces a high concentration of avalanches. [Lea96]

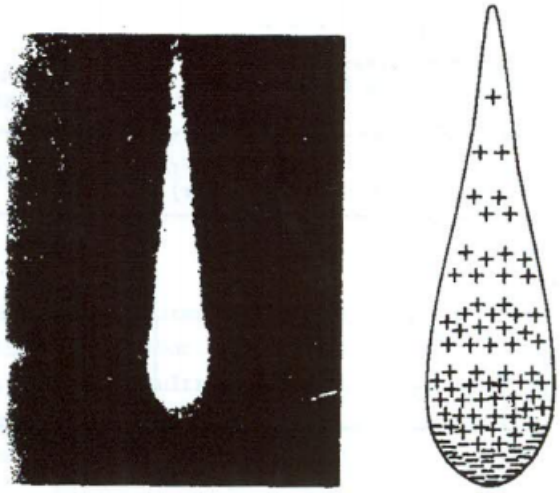

Figure 3.1: Drop like shape of avalanched positive and negative ions. The positive charges are forced to drift to the cathode plates and leave a tail of positive charges. [Leo94]

Avalanches occur when the drift electrons gain enough energy to ionize. When the electron is moving within a constant electric field it will interact with the gaseous medium. The mean free path between interactions can be defined as α^{-1}, where α is known as the Townsend coefficient. Considering a distance between collisions as dx for n numbers of electrons at the point of collisions, the increase in the ionized electrons will be

$$dn = n\alpha dx \tag{3.2}$$

Assuming the Townsend coefficient is constant the differential equation is easily integrated to give

$$M = \frac{n}{n_o} = e^{\alpha x} \tag{3.3}$$

M is defined as the multiplicity factor for electron avalanches. When considering the anode wire's radial electric field the Townsend coefficient is then a function of distance $\alpha = \alpha(x)$ [Sau76]. The multiplicity is generalized for both fields as,

$$M = exp(\int_{x_1}^{x_2} \alpha(x)dx) \tag{3.4}$$

3.2 Particle Tracks

The VDCs can detect artefacts of the charged particle's track geometry by means of ionization. The ionized particles continue to ionize through avalanching [Leo94]. The drift ions follow a single perpendicular line relative to the wire planes. The radial electric field near the wires create a non-linear geodetic path for the ions as in Figure 3.2. Two scintillating panels are placed above and below the VDC and act as time triggers. The timing of the trigger starts when the particle interacts with the scintillator panel and ends when the drift ions trigger the sense wires [J. 03].

The drift time information can be converted to a drift distance. The distances can be used for adjacent wire cells to reconstruct the charged particle's track. The information reconstructed will include the local angle θ and xy position data for momentumand reaction scattering angle calculations.

The track reconstructed is done completely by computational methods. The VDC chamber is implemented as partitioned cells, each cell comprises a single wire and equal width. There are possible misfirings or false avalanches which within the VDC causes false signals [K.G00]. These false signals or accidentals act as a constant background in the timing information and majority of it can be subtracted off. Track reconstruction algorithms that minimize the accidental rate are important for the high triggering rate needed for APEX.

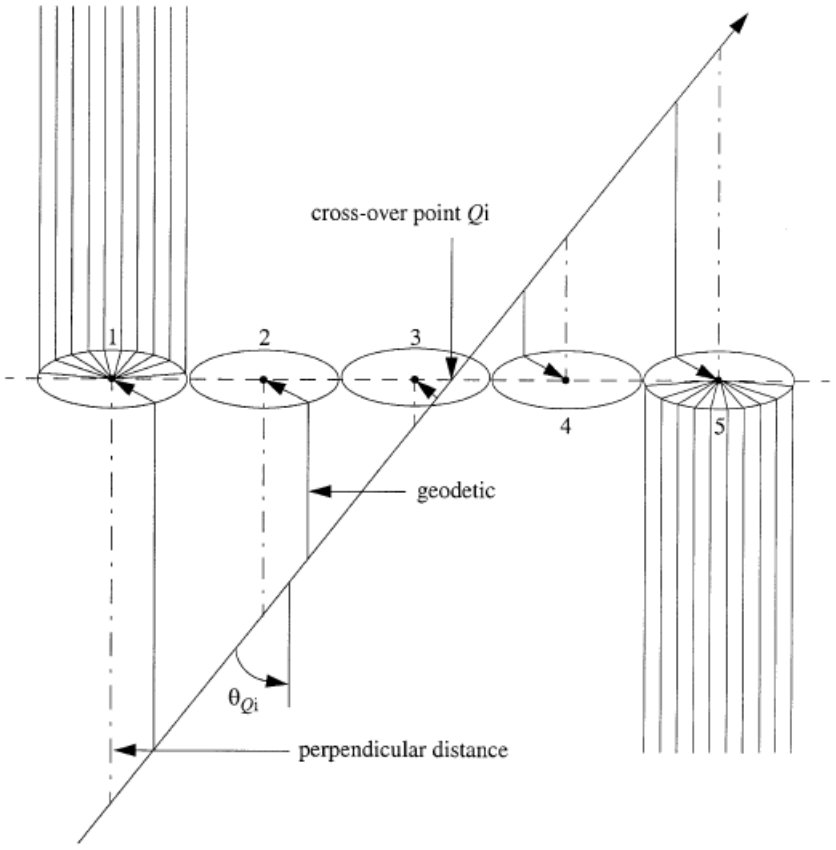

Figure 3.2: A characteristic track for a 5-cell/wire event. The geodetic paths are defined as the paths of least time for the drift electrons. [K.G00]

A track is reconstructed for a set of adjacently fired sense wires or clusters. A cluster is a group of wires fired within a single event with a maximum firing distance of a two wire separation. An event can contain a multitude of clusters, one being of the true particle track while the others are due to accidentals. Each cluster will correspond to its own unique local track. The true track, that is, the track which can be identified as having originated by a reaction in the target can be extracted when the data of both VDCs are compared using a golden track algorithm.

3.3 Time Spectrum

The distribution of arrival times of the drift electrons has a complicated spectrum due to the effects of the radial field. The radial field causes a positional dependence on the mobility and drift velocity of the electrons. Figure 3.3 shows the drift time distribution for electrons drifting within the argon-ethane mixture. The spectrum is in terms of raw TDC channels in which each TDC channel corresponds to a drift time of $.5ns$. The TDC works in common stop mode which causes the TDC channels to increase with decreasing drift times.

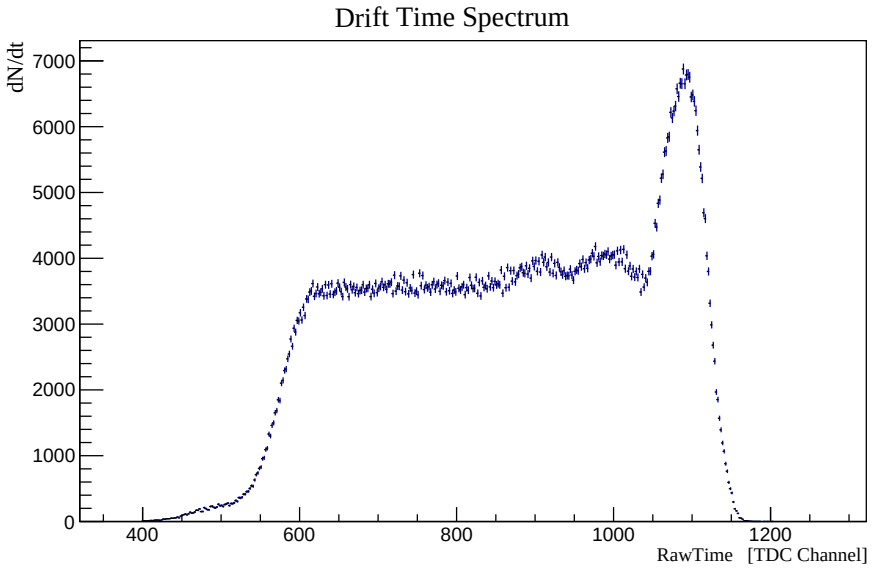

Figure 3.3: Distribution of arrival times of drifting electrons. The arrival times are binned in raw TDC channels (Higher channels correspond to shorter drift times).

The flat plateau in the time spectrum corresponds to regions of constant drift speeds. The flat shape is accomplished when the VDC cell is completely illuminated uniformly with particles such that the number of tracks passing the element dx is given by

$$dN = constant \cdot dx \tag{3.5}$$

When considering the entire spectrum it is easier to look at all of the events per unit time [K.G00], which can be expanded using the chain rule to get equation (3.6).

$$\frac{dN}{dt} = \frac{dN}{ds}\frac{ds}{dt} \tag{3.6}$$

Where ds corresponds to the infinitesimal distance travelled parallel to the field lines. ds/dt id the drift speed for the ions, which is constant except near the sense wires. dN/dt is the effective flux through the drift tracks and is a function of the track angle. The shape of the track at later times (small TDC channels) shows a shoulder dip. The dip is due to larger track angles θ and decreasing drift velocities. The large peak at shorter times (larger TDC Channels) is due to the flux term dominating near the sense wires corresponding to increasing drift velocities [Leo94].

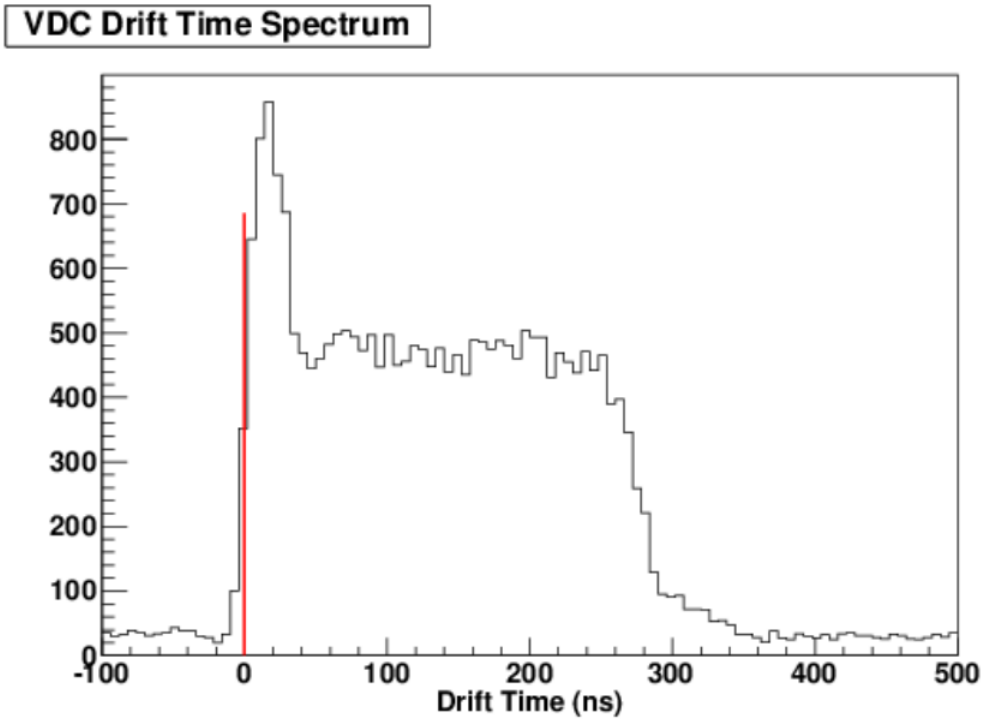

Figure 3.4: Time spectrum of drift velocities in terms of a reference time t_0. The reference time is taken as the time 5-σ away from a Gaussian interpolation over the peak.

The TDC's common stop mode works without a physical reference offset (initial) time t_0. There are various methods used by Hall A in determining a time offset. The first method is to numerically fit a derivative on a channel by channel basis for short time bins dt. The numerical fit can be used to extrapolate a t_0 value distinct for each time spectrum. The alternative method used currently is by fitting a Gaussian distribution over the peak of the spectrum. Five standard deviations (5σ) away from the mean of the Gaussian is used as the reference t_o [J. 03]. In Figure 3.4 the time spectrum is converted to $0.5ns$ time bins using the latter reference determination method.

3.4 Time to Distance Conversion

The complex time spectrum leads to difficulties in converting the drift times of the ions to their respective drift distances. Previously, multiple algorithms have been used in an attempt to properly extract the drift distances. One of these methods involves reconstructing the tracks by simulating the electric fields within the chambers. The simulation program GARFIELD would interpolate a drift time to distance conversion as a third order polynomial [J. 03].

$$d_{GARFIELD}(t) = \alpha_1 t + \alpha_2 t^2 + \alpha 3 t^3 \tag{3.7}$$

The alternative method more commonly used in Hall A is a brute force method. The method is encompassed within their entire global track reconstruction algorithm ECLIPSE. The algorithm takes the local tracks reconstructed from both pairs of (UV)-planes and creates a optimized Golden (Global) track. Figure 3.5 represents the local track reconstruction by projection coefficients onto the wire plane. The algorithm attempts to fit a fourth other polynomial for the time to distance conver-

sion. This is similar to GARFIELD except that the coefficients are not obtained from simulations but rather from angular dependence brute force comparison.

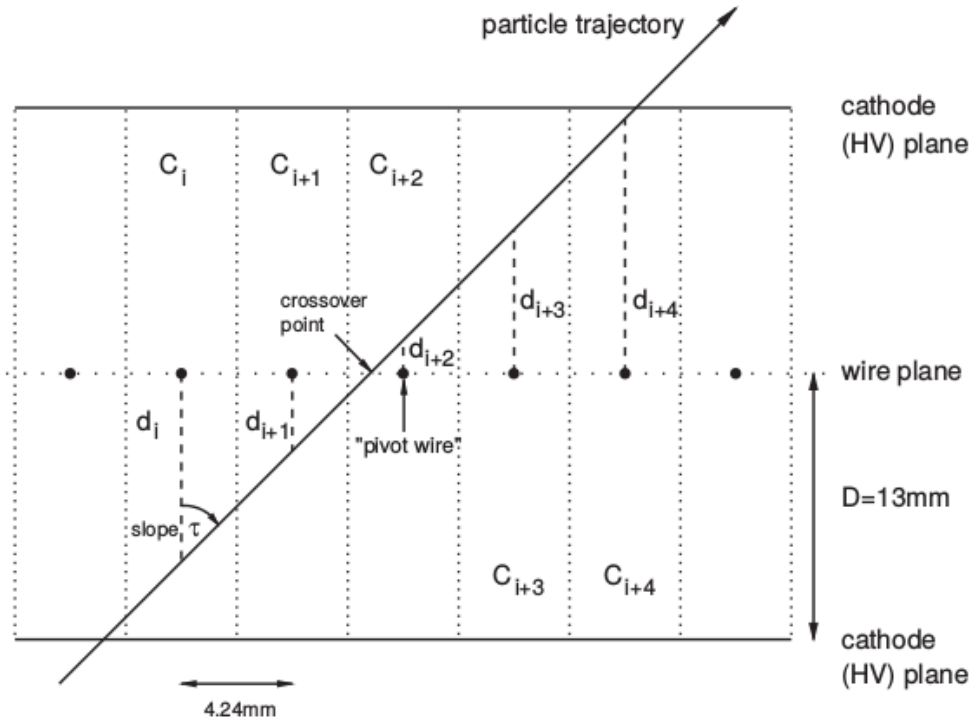

Figure 3.5: Hit cluster pattern on adjacent wires. The distances are perpendicular projections onto the anode wire plane. [J. 03]

3.5 New Algorithm

This thesis discusses the analysis of track reconstruction through an alternative reconstruction algorithm. The new algorithm implemented is based on an old method of velocity look-up tables [Woj15]. The algorithm integrates the time spectrum over time increments. The method is based on the relationship between the time spectrum dN/dt and the ion drift velocities ds/dt. By using equation (3.6) the drift velocity is defined in equation (3.8).

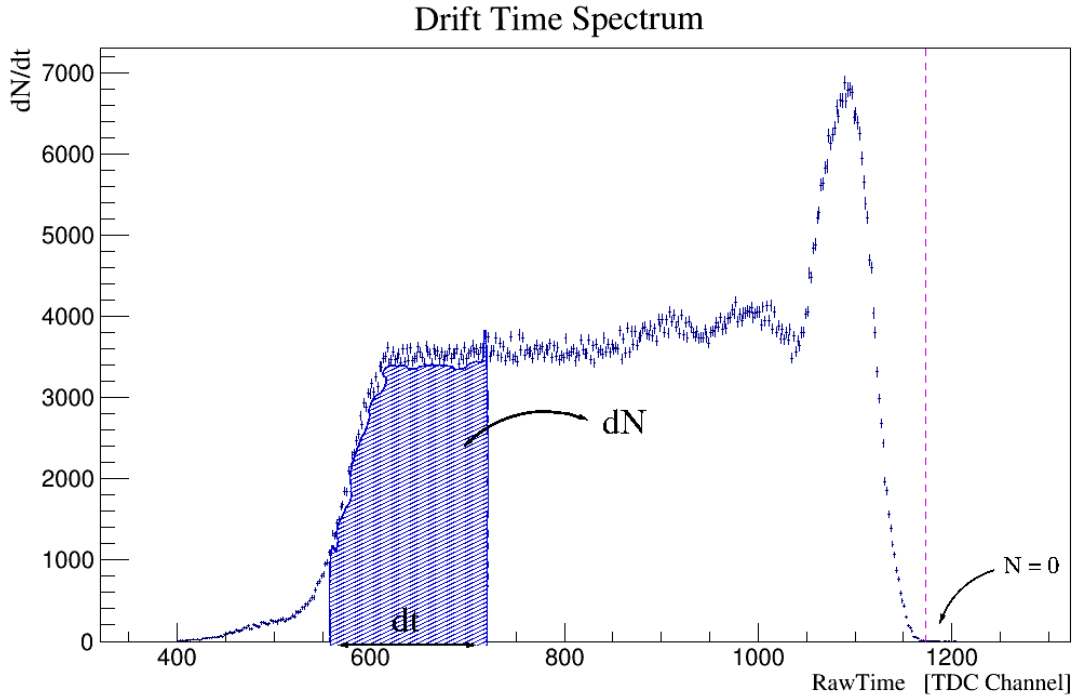

Figure 3.6: Schematic of bin-by-bin integration of the new algorithm. The first non-zero bin integrated is used as a more physical time offset

$$v(t) = \frac{dx}{dN}\frac{dN}{dt} \approx \Phi \frac{d(N^{tot} - N^{ac})}{dt} \tag{3.8}$$

Φ is the corresponding flux of tracks and is considered constant for large samples of events $N_{events} >> large$. The counts N is cut from the background accidentals N_{ac}. The velocity is then a function of counts and time alone. Discrete integration of a specified time step will produce a table of distance conversions, equation (3.9). [Woj15]

$$x(\tau) = \int_0^\tau v(t)dt \approx \int_0^\tau \Phi \frac{d(N^{tot} - N^{ac})}{dt} dt = \Big(x_n\Big) \tag{3.9}$$

The flux Φ is unknown but can be normalized by using the dimensional constraints of the wire chamber. Φ is assumed to be unity as the algorithm produces the look-up

table. The table's distances are then scaled to the chamber's width.

$$\Phi \cdot \sum_{n}^{N} \left(x_n \right) < 14.52mm \tag{3.10}$$

The constructed look-up table is then interpolated with a cubic spline. The interpolated function acts as a drift time to distance (TTD) conversion.

3.6 Diagnostics

Diagnostics checks must be analyzed to ensure that the VDC is properly functioning. One possible problem that can show up between independent wires is crosstalk. Crosstalk occurs when the signal received at one wire produces another signal at an adjacent wire.

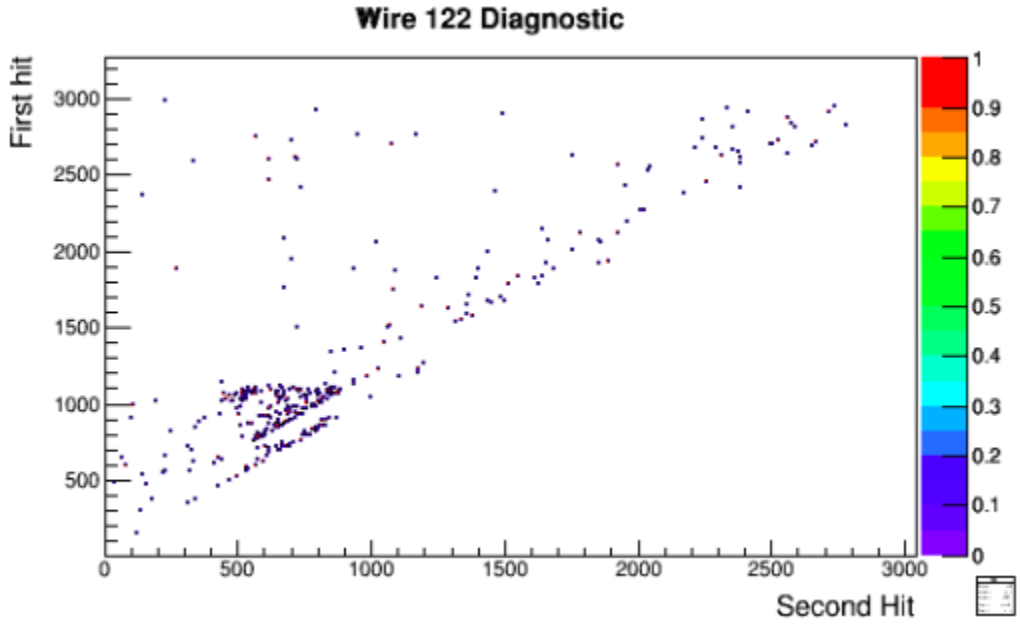

Figure 3.7: Successive hits plotted for wire 122. The geometry should permit events happening at one side of the diagonal.

Figure 3.7 shows the event relationship between two consecutive hits of a wire. The units are of TDC channels corresponding to time. The timing of the first hits

should be less than the timing of the second hit. The plot expresses this constraint with all of its events staying on the half plane where $t_{first} < t_{second}$. An indicator of cross talk between adjacent wires would produce events on the right half plane $t_{first} > t_{second}$.

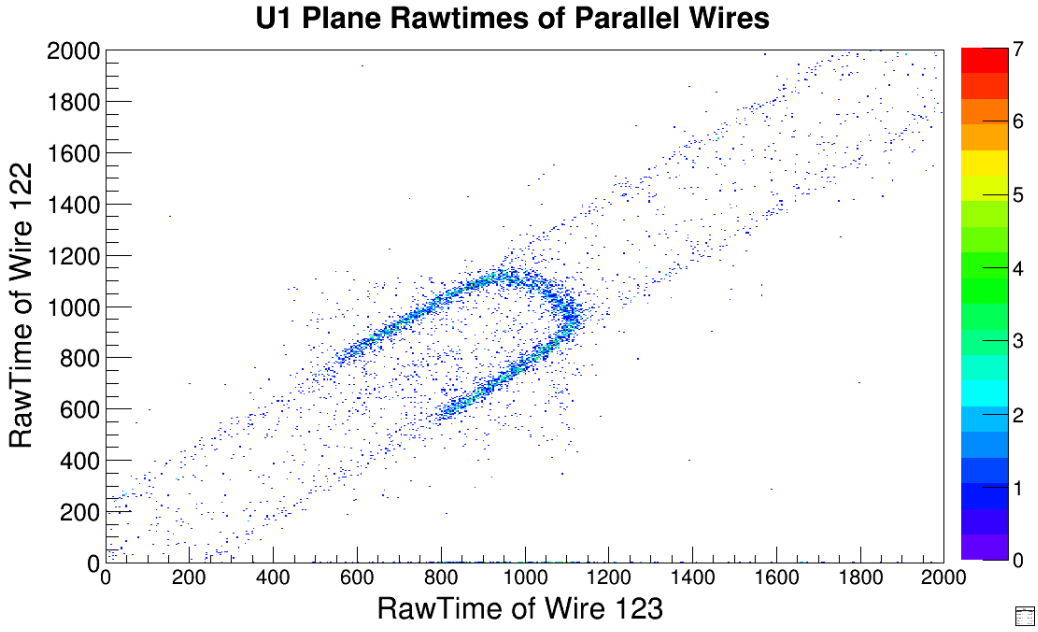

Figure 3.8: 2-dimensional plot of rawtimes between two adjacent wires. The width of the U-shaped region corresponds to the deviation in track angles away from 45°

A more in-depth look at the timing geometry between two adjacent wires can be seen in Figure 3.6. The plot exposes the geometry of hits between two particle tracks. The higher density regions (TDC Channels 800-1200) correspond to projections of each wire's associated rawtime distribution. The outer walls of the U-shape density regions are events in which tracks occur below and over both wires. The connecting upper portion of the U-shape corresponds to events in which the tracks are between both wires. The events which occur inside the U-shape region are not geometrically possible and can be ascribed to crosstalk between the wires.

Chapter 4

DATA ANALYSIS & DISCUSSION

4.1 Drift Distances

The new drift TTD conversion algorithm was tested using APEX test run data. The high triggering rates of 4.0Mhz were used throughout the test run. The new algorithm discussed in the previous chapter was used to analysis the data. Look-up tables were created with the signal data and interpolated to produce a set of TTDs.

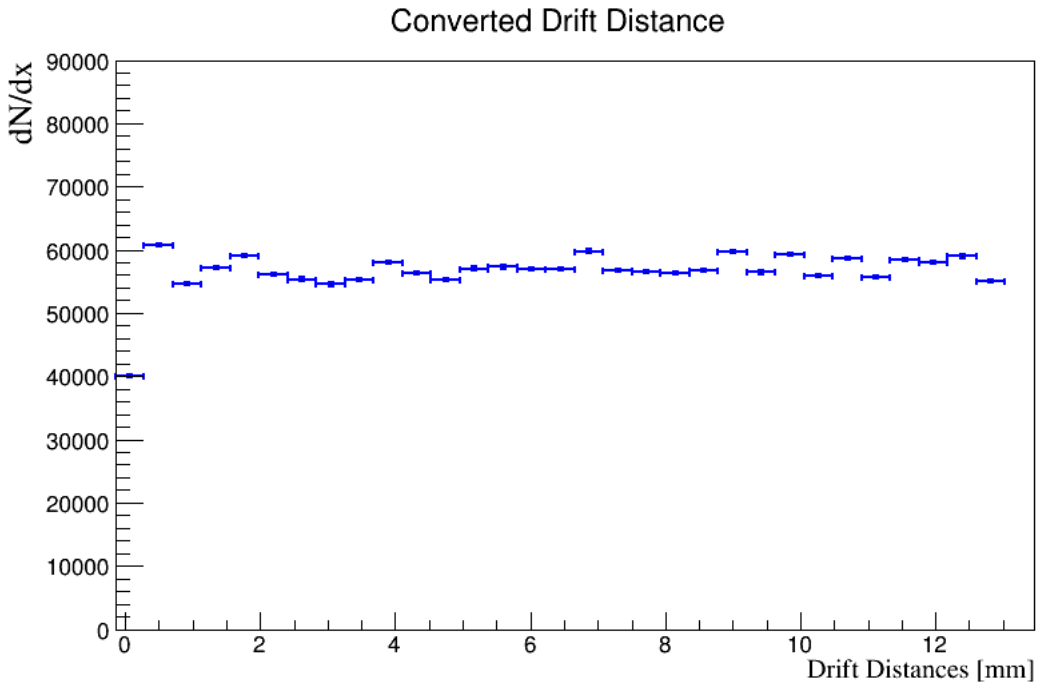

Figure 4.1: The distance spectrum created from the new drift time to distance converter. The spectrum's constant profile is used as a diagnostic.

The geometry of the drift chamber allows us to predict the outcome drift distance distribution. Particle tracks with an average angle of 45° will produce a spectrum of

distances between the chamber separation limitations. When the sample of events is large, the assumption is that flux of tracks surrounds the entire chamber uniformly. With the previous assumption and the parallel plate geometry the distribution should be relatively constant. The TTD algorithm was initially tested by its distance spectrum measurement. Figure 4.1 shows the distribution of drift distances within a TTD resolution of 0.5mm. The spectrum is relatively constant within statistical noise. The distribution was compared to a model constant distance distribution. The root mean square error (RMSE) was found by comparing the ideal and real distributions shown in Appendix (B). The RMSE gives a lower limit on the resolution of the TTD table values in accordance with distance resolutions needed for APEX.

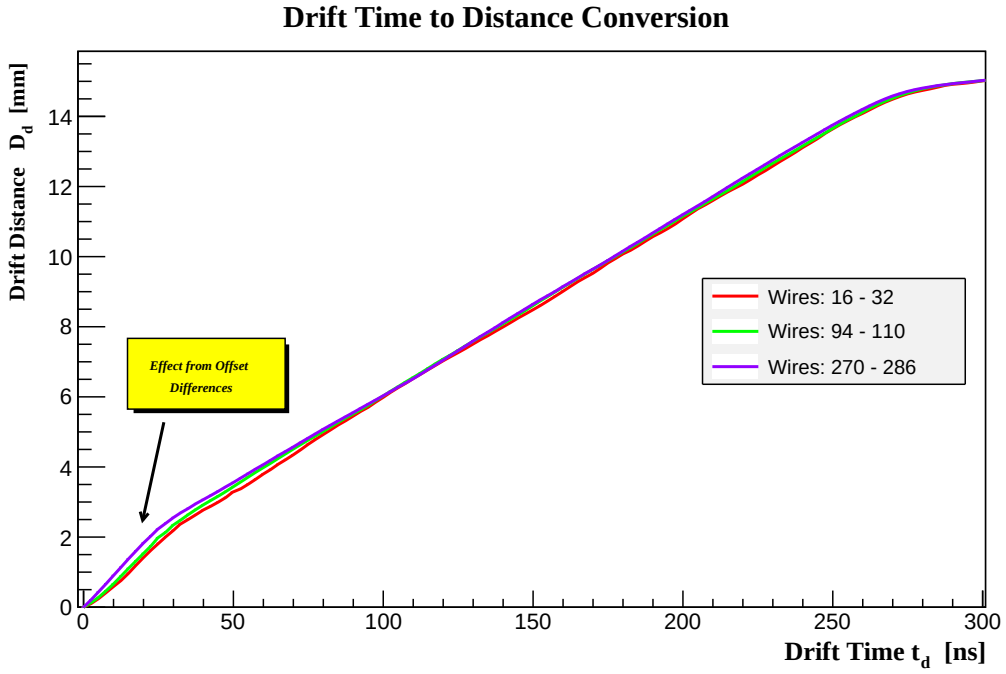

Figure 4.2: Interpolated drift time to distance conversion for multiple 16-wire groups. The time offset effect is seen within the time range of (0.50ns)

The look up table produced by APEX test run data was interpolated with a cubic spline. The cubic spline was an ideal interpolation method due to the lack of rigidity

in the look up table values. The interpolated TTD functions are shown in Figure 4.2. The time offset effects due to the TDC coupling of 16-wire channels discussed in Chapter 4 can be seen in the Figure 4.2. The offset effect causes the drift velocities to vary near the avalanche points in the radial field. The TTD algorithm was adapted to account for the 16-wire group offsets $\chi = f(t_i, t_{offset,j})$. A matrix look up is constructed as in Equation (1.1):

$$\chi_{ij} = T_i + \Phi_j \tag{4.1}$$

T_i is the original TTD look up table partitioned in time. The correction factor Φ_j is the time offset values appended to the table for each wire grouping. The algorithm's routine time is therefore increased since it must sort through an extra dimension of information. Future work would incorporate the TTD algorithm with the Hall-A analyzer framework. This would ideally increase the efficiency of the algorithm.

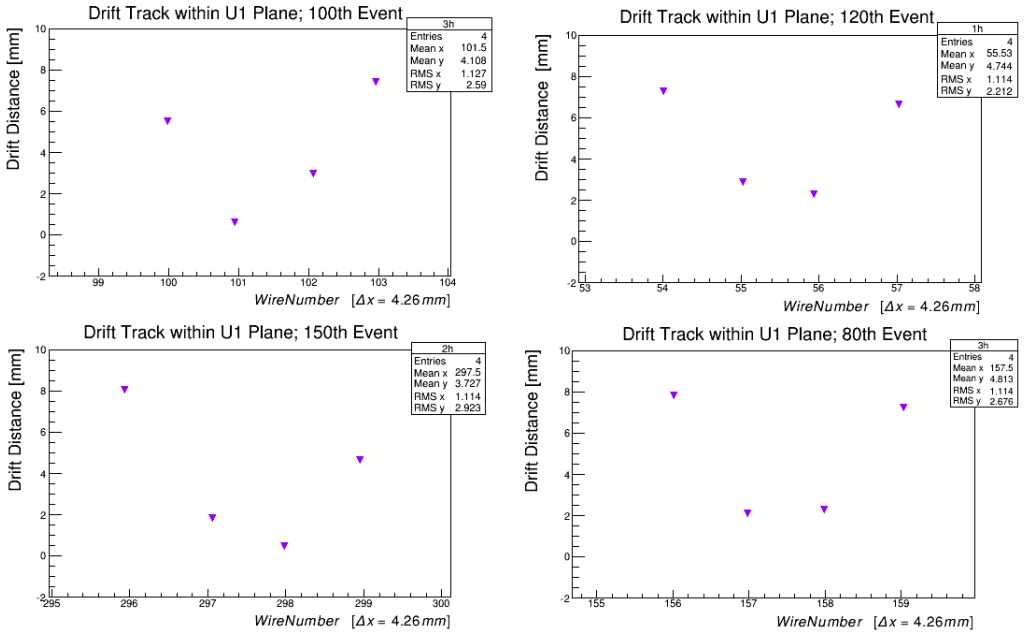

Figure 4.3: Reconstructed particle tracks from four hit cluster data. The 'v-shape' is caused by the positive,definiteness of the drift distance. A turn off point is needed as a reference to reconstruct the proper geometry.

4.2 Mismatching Tracks

The TTD conversion was applied to a select cluster sample for illustration in Figure 4.3. The cluster sizes comprised of four hit events with a maximum wire gap of one. The characteristic 'V-shape' is due to the distances being positive definite. To reconstruct the track geometry the pivot/turn-off point (x_p, d_p) must be extracted. Two linear fits are applied to both sides of V-shape profile. The turn-off point was found by finding the intersection of both interpolated lines:

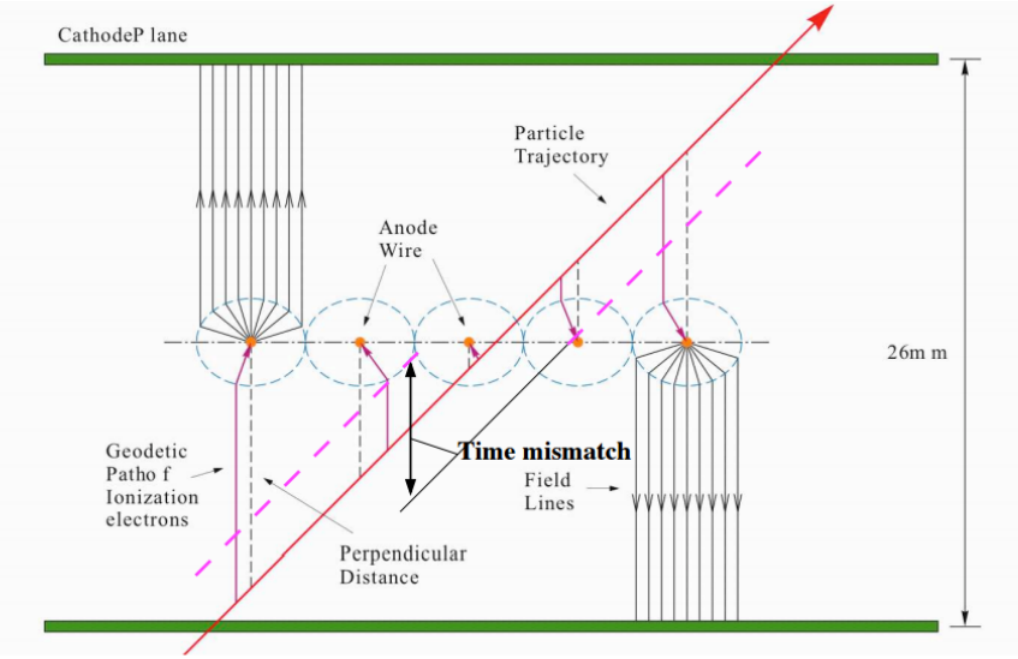

Figure 4.4: Diagram showing the time/distance mismatch effect. The reconstructed track geometry becomes shifted along the turn-off point (wire plane). The effect is related to false tracks corresponding to accidental rates

$$d_{\pm} = \eta_{\pm} \cdot x + \beta_{\pm} \tag{4.2}$$

Where $\pm$ differentiates between the left and right side of the 'v-shape' respectfully. The pivot point was found by setting both interpolated equations equal to each other

$d_+ = d_-$. An algorithm was created to interpolate and reconstruct the pivot point geometry for each cluster within the APEX test run dataset.

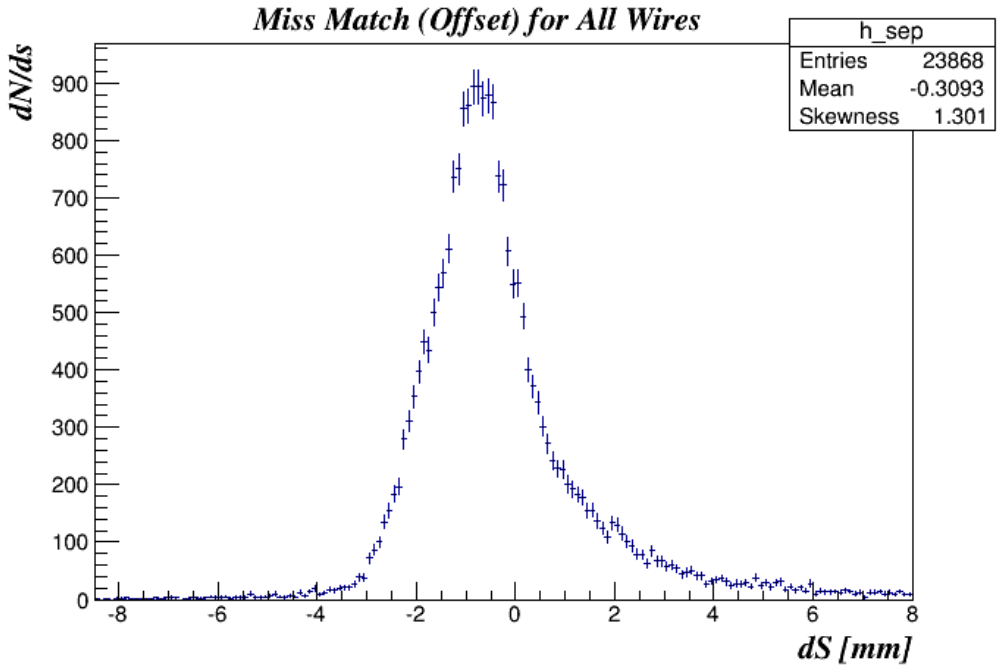

Figure 4.5: Distribution of distance mismatch parameter for all wires. The non-Gaussian shape is non-ideal for any physical cuts to be extracted from it.

The corresponding pivot points extracted did not coincide with the physical wire plane for many of the tracks. A physical criterion was placed within the algorithm to force the pivot point to be along the wire plane (reflection point). The reconstructed tracks with the forced physical condition would exhibit disjointed geometries as in Figure 4.4. The disjointed geometry can be seen as the shifting of the track's trajectory along the wire plane in a parallel fashion. The physicality of the constructed tracks can be judged by the degree of separation or 'shift' along the pivot point. A measure was created for this shift which was called the 'time mismatch' δt or 'distance mismatch' δd depending on which domain the construction is in (time or space domains). The mismatch parameter is taken to be the perpendicular distance from

the constructed pivot point to the physical pivot point along the wire plane. The geometry can be used to extract δs using Equation (4.3).

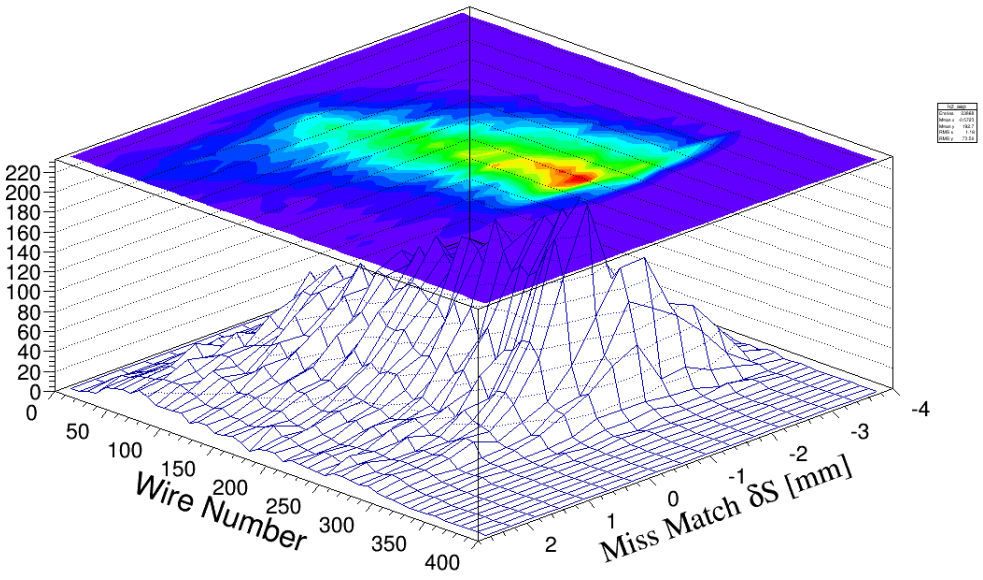

Figure 4.6: 2-dimensional Histogram projection of the miss match parameter as a function of wire distance. The none-constant trend can be ascribed to offset effects in wire groupings

$$\delta s = \sqrt{(x_p - x_{wire})^2 + d_p^2} \tag{4.3}$$

Again (x_p, d_p) corresponds to the reconstructed pivot point and x_{wire} is the true horizontal value for the pivot point. The mismatch parameter was reconstructed for all wire tracks. The distribution of the parameter can be seen in Figure 4.5. The shape of the distribution is a superposition of a Landau and Gaussian. It is skewed from the center of the tracks which does not agree with the assumption that the distances are symmetric. The geometry of the track reconstructions should be uniform and symmetric along the zero point. A two-dimensional histogram was plotted along all wire numbers shown in Figure 4.6. The non-regularity of the histogram shows a

dependence on wire number. This can be explained by the time-offset effect on the 16-wire groups.

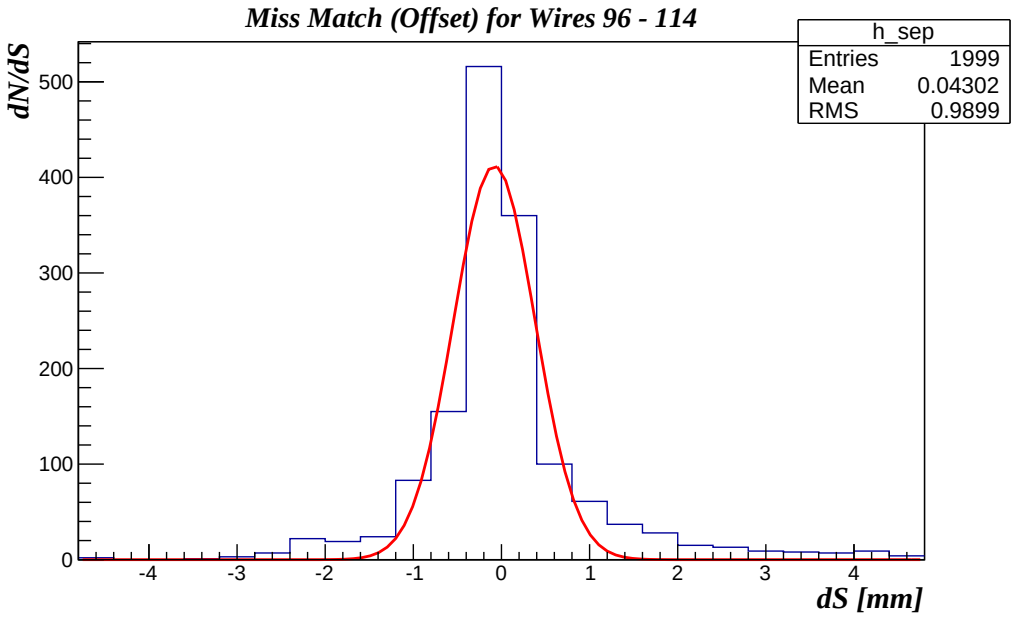

Figure 4.7: Miss Match distribution for a select TDC 16-wire group.

The algorithm was adjusted to compensate for the time-offset effect present in the TTD. The resulting distribution for wires (94-114) is seen in Figure 4.7. The distribution is very close to being centred around the zero point without any skewing. A Gaussian fit was applied to gauge its uniformity around the pivot. The physicality of the track reconstructed can be limited by setting a cut defined by the fitted Gaussian. The cut can be made to limit the accidental/false tracks and lower the accidental rates for APEX. The cut will reduce the tolerance of accidental tracks within the data analysis process. Future work will comprise of increasing the efficiency of the algorithm. The histogram in Figure 4.7 took too long to create for it to be implemented for each data run. A fully integrated algorithm as dedicated class within the Hall-A analyzer would present new tools to increase its efficiency

Chapter 5

CONCLUSION

A new drift time to distance algorithm was developed and used to analyze the APEX test run data. Referring to Figure 4.1 we can see that the extracted distance distribution is uniform and constant. This is in agreement with previous distance converters used by Hall-A. It can also be optimized to produce the needed resolution by increasing the integration bins (Apendix B), although the increased binning produces longer run times for sorting through the look-up table arrays.

The algorithm was successful when the 16-TDC wire groups were considered separately. The matrix form of the TTD conversion can be seen in Figure 4.2. The mismatch parameter defined in Chapter 4 may be used as a cut criteria to reduce accidental triggering. Further work would be to quantify the reduction factor of accidental rates using the mismatch cut.

References

[Ber13] T. Beranek, H. Merkel, and M. Vanderhaeghen, (2013).

[Bjo09] J. D. Bjorken, R. Essig, P. Schuster, and N. Toro, (2009).

[Buc06] W. Buchmuller and C. Ludeling, (2006).

[Che09] C. Cheung, J. T. Ruderman, L.-T. Wang, and I. Yavin, (2009).

[Gol01] H. Goldstein, C. P. P. Jr., and J. L. Safko, *Classical Mechanics (3rd Edition)*, Pearson, 2001.

[Gri04] D. J. Griffiths, *Introduction to Quantum Mechanics (2nd Edition)*, Pearson, 2004.

[J. 03] B. A. J. Alcorna, K. Aniolc, and J. Annandd, Nucl. Instrum. Methods (2003).

[J.D10] R. E. J.D. Bjorken, P. Schuster, and B. Wojtsekhowski, The a0 experiment (apex): Search for a new vector boson a0 decaying to e+e, Technical report, Thomas Jefferson Acclerator Laboratory, 2010.

[Jen13] E. Jensen, *A SEARCH FOR A NEW GAUGE BOSON A'*, Ph. D. Thesis, The College of William and Mary, 2013.

[K.G00] W. B. K.G. Fissum, J. Chen, and D. Dale, Nucl. Instrum. Methods (2000).

[Lan14] J. G. Landry, *CROSS SECTION CALCULATIONS FOR COMPTON SCATTERING FROM THE PROTON NEAR PION THRESHOLD*, Ph. D. Thesis, Mount Allison's University, 2014.

[Lea96] C. Leathers, *Efficiency Measurements on the CEBAF Hall A VDCs*, Ph. D. Thesis, MASSACHUSETTS INSTITUTE OF TECHNOLOGY, 1996.

[Leo94] W. R. Leo, *Techniques for Nuclear and Particle Physics Experiments: A How-to Approach*, Pearson, 1994.

[Mur15] N. J. Murtha, *Investigating Performance of a Scintillation Radiation Detector Design*, Ph. D. Thesis, Saint Mary's University, 2015.

[Ree10] M. Reece1 and L.-T. Wang, (2010).

[Rom14] A. Romanino, *The Standard Model of Particle Physics*, SISSA/ISAS, 2014.

[Sau76] F. Sauli, Principles of operation of multiwire proportional and drift chambers, Technical report, CERN, 1976.

[Wec96] R. H. Wechsler, *Drift-Time Properties of CEBAF Hall A Vertical Drift Chamber*, Ph. D. Thesis, MASSACHUSETTS INSTITUTE OF TECHNOLOGY, 1996.

[Woj15] B. Wojtsekhowski, private communication, 2015.

Appendix A
ECLIPSE Drift Time to Distance Algorithm

The local track for a set of (UV) wire planes is geometrically reconstructed by a brute force fourth-order polynomial fit. The polynomial coefficients are a function of the track angle θ.

$$P(\theta, t) = a_3(\theta)t^3 + a_2(\theta)t^2 + a_1(\theta)t + a_0(\theta) \tag{A.1}$$

A linear reference distance is used D_d. The distance is taken as the mean drift velocity in the chamber. For a argon-ethane mixture the mean drift velocity is $50\mu m/ns$. The algorithm defines two recursive functions in terms of the fit coefficients.

$$P' = \frac{1}{tan(\theta)}(P'_{n-1} + a'_n) \tag{A.2}$$

$$P'' = \frac{1}{tan(\theta)}(P''_{n-1} + a'_n) \tag{A.3}$$

The Recursive process is iterated over a loop equal to the order of the polynomial. Two final polynomials can be constructed in terms of the recursively found coefficients

$$P' = P'_3(\theta, a'_n) + a'_0 \tag{A.4}$$

$$P'' = P''_3(\theta, a''_n) + a''_0 \tag{A.5}$$

The algorithm then computes a drift distance D'_d dependant on which side of the approximate distance $D_d = 50\mu m/ns \cdot t$ value the polynomial P' lies on. The following is the if-else statement determination of the distance.

$$if \quad D_d < P' \quad \rightarrow \quad D'_d = D_d(1 + \frac{P''}{P'}) \tag{A.6}$$

$$else \quad D_d > P' \quad \rightarrow \quad D'_d = D_d \cdot P'' \tag{A.7}$$

Appendix B
Error and Resolution of TTD Conversion

The converted position distribution has a non-constant spectrum due to statistical fluctuation and error in the interpolated tables. The position resolution can be obtained by modelling the root mean square error (RMS). Two distributions can be are considered, the ideal constant positional spectrum dN/dx and the actual functional spectrum dN/dy. Where y is the position coordinate in the non-ideal system.

$$(ideal) \qquad \frac{dN}{dx} = \mathcal{C} \in \mathcal{R} \tag{B.1}$$

$$(actual) \qquad \frac{dN}{dy} = f(y) \tag{B.2}$$

Applying the chain rule on the differentials to find a relationship between both coordinate systems

$$\frac{dN}{dy} = \frac{dN}{dx}\frac{dx}{dy} = \mathcal{C} \cdot \frac{dx}{dy} \tag{B.3}$$

This shows that the actual distribution can be modelled in terms of a functional distribution dx/dy. Since the statistical fluctuations have been primarily periodic, a general trigonometric model is used.

$$\frac{dx}{dy} = 1 + \alpha \cdot cos(\frac{2\pi y}{\lambda}) \tag{B.4}$$

This modelling distribution can be integrated to give a constraint relationship between the ideal and actual positional coordinates.

$$x(y) = \int \frac{dx}{dy} dy$$

$$x(y) = y + \alpha\frac{\lambda}{2\pi} \cdot cos(\frac{2\pi y}{\lambda}) + C \tag{B.5}$$

The RMS (variance) relationship is can be evaluated as the square expectation value of the differences in the two models.

$$\sigma^2 = \langle (x - y)^2 \rangle \tag{B.6}$$

$$\sigma^2 = \langle (y + \alpha\frac{\lambda}{2\pi} \cdot cos(\frac{2\pi y}{\lambda}) + C - y)^2 \rangle$$

Normalize the distribution height ($C = 1$) without loss of generality.

$$\sigma^2 = \langle (\alpha \frac{\lambda}{2\pi} \cdot cos(\frac{2\pi y}{\lambda})^2 \rangle$$

The average of $cos^2(\phi)$ is equal to a half $\langle cos^2(\phi) \rangle = \frac{1}{2}$. The upper limit on the error (variance) can be computed as

$$\sigma = \frac{\alpha\lambda}{2\sqrt{2}\pi} \tag{B.7}$$

Appendix C
GitHub Account and Developed Thesis Code

The code created for the thesis analysis is too large to be included (and a waste of paper). The below GitHub account is linked to a thesis repository, hosting the analysis code.

https://github.com/Linthorne/Thesis.git

RELEASE FORM

To be bound into all copies of theses submitted to
Saint Mary's University

AUTHORITY FOR LIBRARY TO REPRODUCE

(To be signed by author)

I hereby authorize the making of copies of this thesis for study purposes.

(Strike out the two statements which are not appropriate.)

A. Without restriction.

B. With the restriction that until_____
_____Department is required.
(maximum period: five years)

C. With the restriction that until_____
(maximum period: five years)
the written approval of the author is required.

Signed_____
Date_____